Nanoscale

PAPER

View Article Online
View Journal | View Issue

Published on 22 March 2019. Downloaded by SHANXI INSTITUTE OF COAL on 6/14/2019 4:02:46 AM.

Check for updates

Cite this: *Nanoscale*, 2019, **11**, 8037

Morphology evolution of fcc Ru nanoparticles under hydrogen atmosphere†

Lili Liu, [a,b] Mengting Yu,[a,b] Bo Hou,[a] Qiang Wang, *[a] Beien Zhu,*[c] Litao Jia[a,d] and Debao Li*[a,d]

Received 22nd February 2019,
Accepted 22nd March 2019

DOI: 10.1039/c9nr01611b

rsc.li/nanoscale

Tuning the morphology and structural evolution of metal nanoparticles to expose specific crystal facets in a certain reaction atmosphere is conducive to designing catalysts with a high catalytic activity. Herein, coverage dependent hydrogen adsorption on seven fcc Ru surfaces was investigated using density functional theory (DFT) calculations. The morphology evolution of the fcc Ru nanoparticles under the reactive environment was further illustrated using the multiscale structure reconstruction (MSR) model, which combines the DFT results with the Fowler–Guggenheim (F–G) adsorption isotherm and the Wulff construction. At constant pressure, the shape of a fcc Ru nanoparticle changes from a rhombic dodecahedron to a truncated octahedron with an increase of the temperature. More importantly, the desired Ru morphology, with abundant open facets, was predicted to occur at a high temperature and low pressure. Our results provide an insightful understanding of the reshaping of Ru nanoparticles during real reactions, which is crucial for its rational design for use as a nanocatalyst.

1. Introduction

Fabricating metal nanocrystals with well-controlled shapes endows them with important applications in heterogeneous catalysis, such as in the electrocatalytic reaction,[1–4] Fischer–Tropsch synthesis (FTS),[5,6] ammonia synthesis,[7,8] and the hydrogenation reaction,[9,10] owing to their unique chemical and physical properties. In recent years, remarkable progress has been made in understanding the activity of catalysts, which greatly depends on the arrangement manner of the surface atoms and the number of dangling bonds on different crystal planes.[11–13] Control of the crystal structures to expose specific facets has been considered to be of primary importance for achieving the desired activity in heterogeneous catalysts.[14–16] However, tuning the morphology and structure of the catalysts under reaction conditions is still a challenging task.

The perturbations of the synthesis environment are critical to the formation of metal nanocrystals with different shapes and surface structures,[17–19] and even their catalytic performance.[20–22] To gain an insight into the complex process, substantial efforts have been devoted towards exploring the shape evolution of metal nanocrystals under reactive environments. *In situ* scanning tunneling microscopy (STM) studies performed by Banerjee *et al.* revealed a remarkable structure reconstruction when Co single crystals were exposed to syngas under FTS conditions of 3 bar and at 383 K.[23] Simonsen *et al.* reported that Pt nanoparticles had size-dependent morphologies after sintering in an oxidizing environment by using atomic scale transmission electron microscopy (TEM) observations.[24] By combining experiments with theoretical analysis, Zhang *et al.* found that cubic Pd nanoparticles became truncated at the edges under 1 bar O_2 (T = 200 °C), whereas under 1 bar H_2 (T = 300 °C) they were transformed into a truncated shape enclosed by (100), (110) and (111) facets.[18] However, studying all of the catalytic systems using *in situ* experiments is not possible owing to the technical limitations and high cost. Therefore, it is necessary to study the structure and morphology of metal nanocrystals in real conditions by means of theoretical approaches. A lot of calculations indicate that the reaction environment can affect the proportion of the exposed surface of the metal nanoparticles and induce shape transformation.[25–27] For example, Zhu *et al.* observed that Pt, Pd, Cu, and Au nanoparticles undergo different shape variations in CO and NO gas environments, where CO adsorption on Pt nanoparticles leads to more open (110) facets and step sites that favor the improvement of the activity.[28] Wang and co-workers investigated the effect of the pretreatment

[a]State Key Laboratory of Coal Conversion, Institute of Coal Chemistry, Chinese Academy of Sciences, Taiyuan, Shanxi 030001, China. E-mail: wqiang@sxicc.ac.cn, dbli@sxicc.ac.cn
[b]University of Chinese Academy of Sciences, Beijing 100049, China
[c]Shanghai Advanced Research Institute, Chinese Academy of Sciences, Shanghai, 201210 China. E-mail: zhubeien@sinap.ac.cn
[d]Dalian National Laboratory for Clean Energy, Dalian 116023, China

†Electronic supplementary information (ESI) available. See DOI: 10.1039/c9nr01611b

Published on 22 March 2019. Downloaded by SHANXI INSTITUTE OF COAL on 6/14/2019 4:02:46 AM.

atmosphere on the surface stability and morphology evolution on the exposed facets of the Fe phase. They found that the most favorable exposed Fe(100) surface under N_2 atmosphere can result in a significant increase in ammonia synthesis activity,[25] whereas, under H_2 atmosphere the most exposed surface is that of Fe(110) with the lowest activity.[29] In addition, it has also been reported that the equilibrium shape of a Mo single crystal under H_2 reduction atmosphere depends on the temperature, which exposes (110), (211) and (100) facets only at high temperature.[30] In short, the desired activity and selectivity could be achieved by tuning the crystallographic orientation of a nanocatalyst under different reactive gas conditions.

Recently, Ru nanoparticles with fcc structures[31–33] have triggered significant research interest owing to the size dependence of the catalytic activity compared to conventional hcp Ru, that is the fcc Ru nanoparticles were more efficient with increasing particle size (>3.0 nm).[34–36] The superior activity of fcc Ru, with more active crystal surfaces exposed, has been further proposed in many catalytic reactions, such as the hydrogenation reaction,[37,38] N_2 activation,[39] ammonia synthesis,[40] the oxygen evolution reaction,[41] and FTS.[42] These reactions usually involve interactions between the Ru nanoparticles and the surrounding gas constituents (typically hydrogen), which may become strong enough to change the shape and structure of the nanoparticles. Significant attention regarding the morphology evolution of the Ru nanoparticles has been focused on achieving the desired catalysts with a greater reactivity and a higher active-site density.[43,44] Yin *et al.* prepared Ru nanocrystals with different morphologies using a hydrothermal approach and found that the thermolysis of oxalate species led to the shape evolution of Ru nanocrystals, from prisms to capped columns.[45] The subsequent CO selective methanation tests on these Ru nanocrystals indicated that nanoplates have a much better CO selectivity than spherical nanoparticles. In addition, fcc Ru catalysts were found to have a higher activity with denser and more favorable active sites compared with the hcp Ru catalysts in the aqueous-phase FTS.[42] Consequently, investigation of the structure and morphology evolution of fcc Ru under gas atmosphere is necessary to achieve the desired Ru nanocrystals with abundant active facets under realistic conditions.

Ru-Based FTS catalysts are usually comprised of Ru in its metallic form, prior to the experiment, the catalyst is reduced under hydrogen atmosphere.[46–48] Thus, an understanding of the equilibrium morphology evolution of the Ru nanoparticles under hydrogen environments is critical for tuning of the catalytic activities. Herein, we present a systematic density functional theory (DFT) study to determine hydrogen adsorption configurations on different Miller index surfaces of fcc Ru nanoparticles at different coverages. Using Fowler–Guggenheim (F–G) adsorption isotherms and Wullf construction, we observed how the morphology of the catalyst changes when it is exposed to the hydrogen environment. In addition, the effect of hydrogen on the surface stability and the morphology evolution of fcc Ru depending on the temperature and pressure were also considered. To date, this is the first systematic attempt to explain the respond of fcc Ru nanoparticles to a hydrogen atmosphere at the atom level. It also illuminates the intrinsic relationship between the morphology (crystallographic facet), reduction atmosphere, temperature, and H_2 partial pressure.

2. Computational models and methods

2.1 Models

Calculations of the fcc Ru bulk crystal structure with a *k*-point mesh of 5 × 5 × 5 gave a lattice constant of 3.83 Å, this is in good agreement with the previous experimental result (3.71 Å)[38] and the theoretical value (3.82 Å).[42] Hydrogen adsorption was investigated using the (110), (100), (111), (311), (211), (221) and (321) surfaces within the $p(2 \times 3)$, $p(3 \times 3)$, $p(3 \times 3)$, $p(2 \times 3)$, $p(1 \times 3)$, $p(3 \times 1)$ and $p(2 \times 2)$ supercells, respectively. The facets of (110), (311) and (221) were simulated using three layers slabs, and the rest adopted four layers. All of the adsorbed H atoms and the topmost two layers were relaxed, and the rest of the bottom layers were fixed in their bulk positions. The Brillouin zone sampling was carried out using a Monkhorst–Pack[46] *k*-point grid of 5 × 5 × 1 in all of the calculations. A vacuum region of 15 Å was employed to avoid interactions between the periodically repeating slabs.

The structure models of Ru(110), Ru(100), Ru(111), Ru(311), Ru(211), Ru(221) and Ru(321) surfaces, as well as the considered possible hydrogen adsorption sites, are shown in Fig. S1.† The (110) surface has top (T), short-bridge (SB), long-bridge (LB), three-fold hollow ($3F_1$, $3F_2$), and four-fold hollow (4F) sites. The (100) surface has top (T), bridge (B), and four-fold hollow (4F) sites. The (111) surface has top (T), bridge (B), face-cubic centered (F), and hexagonal close-packed (H) sites. Obviously, the high Miller index surfaces provide more available adsorption sites. The (311) surface has nine adsorption sites: two top (T_1, T_2), four bridge (B_1, B_2, B_3, B_4), two three-fold hollow ($3F_1$, $3F_2$), and one four-fold hollow (4F) sites. The (211) surface has twelve adsorption sites: three top (T_1, T_2, T_3), five bridge (B_1, B_2, B_3, B_4, B_5), and four three-fold hollow ($3F_1$, $3F_2$, $3F_3$, $3F_4$) sites. The (221) surface has seventeen adsorption sites: four top (T_1, T_2, T_3, T_4), six bridge (B_1, B_2, B_3, B_4, B_5, B_6), and seven three-fold hollow ($3F_1$, $3F_2$, $3F_3$, $3F_4$, $3F_5$, $3F_6$, $3F_7$) sites. The (321) surface has sixteen adsorption sites: five top (T_1, T_2, T_3, T_4, T_5), six bridge (B_1, B_2, B_3, B_4, B_5, B_6), and five three-fold hollow ($3F_1$, $3F_2$, $3F_3$, $3F_4$, $3F_5$) sites.

2.2 Methods

All spin-polarized DFT calculations were carried out using the Vienna *ab initio* simulation package (VASP).[47,48] The interaction between the ionic cores and the electrons was described using the projector-augmented wave (PAW) method.[49] The generalized gradient approximation (GGA) with a Perdew–Burke–Ernzerhof (PBE)[50] functional was used to calculate the exchange–correlation energy. The energy cutoff for the plane-

 This journal is © The Royal Society of Chemistry 2019

Published on 22 March 2019. Downloaded by SHANXI INSTITUTE OF COAL on 6/14/2019 4:02:46 AM.

wave basis set was set to 400 eV. The structures were optimized using energy and force convergence limits equal to 10^{-5} eV per atom and 0.03 eV $Å^{-1}$, respectively. The adsorption energy for hydrogen adsorption on the surface is determined by:

$$E_{ads} = E[\{nH\}/Ru(hkl)] - E[Ru(hkl)] - \frac{1}{2}nE[H_2] \quad (1)$$

where $E[\{nH\}/Ru(hkl)]$ is the total energy of the Ru surface with nH adsorption, $E[Ru(hkl)]$ is the total energy of the corresponding clean Ru(hkl) surface, $E[H_2]$ is the total energy of an isolated hydrogen molecule in the gas phase, and n is the number of H atoms. A negative E_{ads} indicates that adsorption is favored.

For the H stepwise adsorption at different coverages, the H-covered Ru surfaces were modeled by adding H atoms one by one on the most stable configurations. The stepwise adsorption energy is used to identify the saturated coverage, defined as

$$\Delta E_{ads} = E[\{(n+1)H\}/Ru(hkl)] - E[\{nH\}/Ru(hkl)] - \frac{1}{2}E[H_2]. \quad (2)$$

where a positive ΔE_{ads} represents a saturated coverage with the numbers of H atoms being n. At each coverage, all possible adsorption sites of newly added H atoms were tested to yield the most favorable adsorption configuration based on the most stable structure of the previous coverage.[27] The stable configurations of hydrogen adsorption at different coverage to saturation on each Ru surface and the corresponding stepwise adsorption energies are given in the ESI (Fig. S2–S8†).

According to the Wulff theory, the fcc Ru is assumed to be in thermodynamic equilibrium with the surrounding gas, and the most stable adsorption configuration is the one that minimizes the surface free energy. The surface tension for the Ru surface model with H adsorption is revised as the interface tension γ_{hkl}^{int}, which can be described using the following formula:[28]

$$\gamma_{hkl}^{int} = \gamma_{hkl} + \theta(E_{ads} - k\theta/A_{at}) \quad (3)$$

where θ is the adsorption coverage of the H atoms on the Ru surfaces, k is the fitted lateral interaction energy between the adsorbed H atoms, which is the average adsorption energy dependent (Fig. S9†), A_{at} is the area of the exposed plane per surface atom, and γ_{hkl} represents the surface tension of the pure Ru metal surface, which is expressed as:

$$\gamma_{hkl} = [E_{Ru(hkl)} - n_{Ru}E_{Ru(bulk)}]/2A \quad (4)$$

where $E_{Ru(hlk)}$ and $E_{Ru(bulk)}$ are the total energies of the Ru(hkl) surface and the bulk Ru, respectively, n_{Ru} denotes the number of bulk units in the system, and $2A$ represents the total surface area of the two equilibrium surfaces (top and bottom surfaces).

To construct the morphology of Ru nanoparticles under the H_2 environment, the calculation scheme we adopted is the multiscale structure reconstruction (MSR) model that has been widely applied in many catalytic systems.[51–53] The MSR model combines the DFT calculations with Wulff construction, and the F–G adsorption isotherm, giving a quantitative description and prediction of the equilibrium shapes of metal nanoparticles at a certain temperature and gas pressure. Therefore, we considered the effect of hydrogen conditions on the morphology changes of Ru nanoparticles.

The coverage θ of the dissociative adsorbed H atoms on Ru surfaces can be described using the F–G adsorption isotherm, including the repulsion interactions between the adsorbates:

$$PK = \frac{\theta^2}{1-\theta^2}e^{-c\theta} \quad (5)$$

$$c = k/RT \quad (6)$$

where P is the pressure of H_2, T is the temperature, R is the gas constant and K is the adsorption equilibrium constant which is defined by:

$$K = \exp\left(-\frac{\Delta G}{RT}\right) = \exp\left(-\frac{E_{ads} - T(S_{ads} - S_{gas})}{RT}\right) \quad (7)$$

where S_{ads} and S_{gas} are the entropies of the adsorbed and gas-phase molecules, respectively. The thermodynamic parameter, S_{gas}, was obtained from the NISTJANAF Thermochemical tables[54] (see Fig. S10†) and S_{ads} is assumed to be zero.

3. Results and discussion

3.1. Morphology and surface stability of fcc Ru under vacuum

The equilibrium morphology of fcc Ru under vacuum was investigated based on the Wulff construction, as shown in Fig. S11.† The calculated surface energies and referenced literature values[42] are listed in Table 1. The constructed fcc Ru belongs to the O_h point group with a high symmetry and contains seven different facets, shown as a regular truncated octahedron, which is consistent with the electron diffraction pattern of fast Fourier transform.[38]

Under vacuum, the equilibrium shape of the Ru nanoparticle is covered predominantly with eight close-packed (111) facets, accounting for about 64.2% of the total surface area. Among the exposed facets, the closed-packed (111) facet has the lowest surface energy of 141 meV $Å^{-2}$ and is the most thermodynamically stable facet, which is in line with the previous surface distribution of the truncated octahedral fcc Ru nanoparticle[55] and the closed-shell fcc structure Ru_{19}^- cluster.[56] The (311) and (100) facets with relatively larger surface energies of 174 and 175 meV $Å^{-2}$, cover about 8.2% and 9.2% of the total surface area, respectively. The other three exposed facts (211), (221) and (321) with γ = 167, 158 and 170 meV $Å^{-2}$, cover the rest of the fractions of surface distribution, namely, 2.3%, 13.0%, and 3.1%, respectively. The (110) surface does not appear on the Ru nanoparticle under vacuum. On the basis of surface energies, the stability order of

Published on 22 March 2019. Downloaded by SHANXI INSTITUTE OF COAL on 6/14/2019 4:02:46 AM.

Table 1 Calculated surface energies and distribution of facets on fcc Ru based on the Wulff construction

Facet	Slab	Slab parameters (Å)	Surface energy (meV Å^{-2})		A_{at} (Å^2)	Surface area proportion (%)
			This work	Ref. 42		
(110)	$p(2 \times 3)$	$a = 7.66$, $b = 8.12$	167	170	5.19	0.0
(100)	$p(3 \times 3)$	$a = b = 8.12$	175	184	7.33	9.2
(111)	$p(3 \times 3)$	$a = b = 8.12$	141	145	6.35	64.2
(311)	$p(2 \times 3)$	$a = 9.38$, $b = 8.12$	174	180	6.08	8.2
(211)	$p(1 \times 3)$	$a = 6.63$, $b = 8.12$	167	172	5.99	2.3
(221)	$p(3 \times 1)$	$a = b = 8.12$	158	163	5.50	13.0
(321)	$p(2 \times 2)$	$a = 9.38$, $b = 12.11$	170	174	5.49	3.1

the exposed facets is estimated to be: (111) > (221) > (110) = (211) > (321) > (311) > (100), in which (111) is the most stable surface and (100) is the least stable surface. The results of the surface energies in the present work were consistent with the reported literature,[42] indicating the accuracy and rationality of our calculations.

3.2. Dissociative hydrogen adsorption at different coverage

A well-defined catalyst needs to be first screened by reducing gas (composed primarily of H_2) before the reaction.[57] The dispersion, surface area and particle size of the metal Ru catalyst are usually evaluated by the chemisorption of H_2, which has been proven to be dissociated H atoms on the Ru metal surfaces.[58,59] Thus, it is interesting to investigate the geometric structures and electronic properties of dissociative hydrogen adsorption on Ru surfaces.

For H adsorption on Ru nanoparticles, different hydrogen coverage need to be considered for determining the active sites and surface structures of H adsorption under reaction conditions. As mentioned above, we used a stepwise adsorption method to identify the most stable dissociative hydrogen adsorption configurations at different coverage.[60] The adsorption structures of hydrogen at saturation coverage on each Ru surface are presented in Fig. 1.

The calculated adsorption energies of the favorable adsorption sites for H on each Ru surface at the lowest coverage, as well as the average Ru–H distance, are listed in Table 2. The most stable adsorption sites and corresponding adsorption energies are in line with the results reported in the literature.[42] There are obvious differences in the hydrogen adsorption among these Ru surfaces. At the lowest coverage, the most stable adsorption of one H atom is the SB site on Ru(110), B site on Ru(100), F site on Ru(111), B_1 site on Ru(311), B_1 site on Ru(211), $3F_1$ site on Ru(221) and B_1 site on Ru(321) with the adsorption energies of −0.52, −0.61, −0.60, −0.64, −0.65, −0.62 and −0.59 eV, respectively. It was found that the adsorption strength in the high Miller index surfaces is stronger than that of the low Miller index surfaces, mainly because of the different inherent surface structures. The average bond length between Ru and H increased as expected with the increasing coordination number, for example, from 1.63 Å at the T site to 2.05 Å at the 4F site on the Ru(100) surface (Table 2).

Further addition of H atoms may lead to the migration of H atoms to a more stable adsorption site, owing to the high-cov-

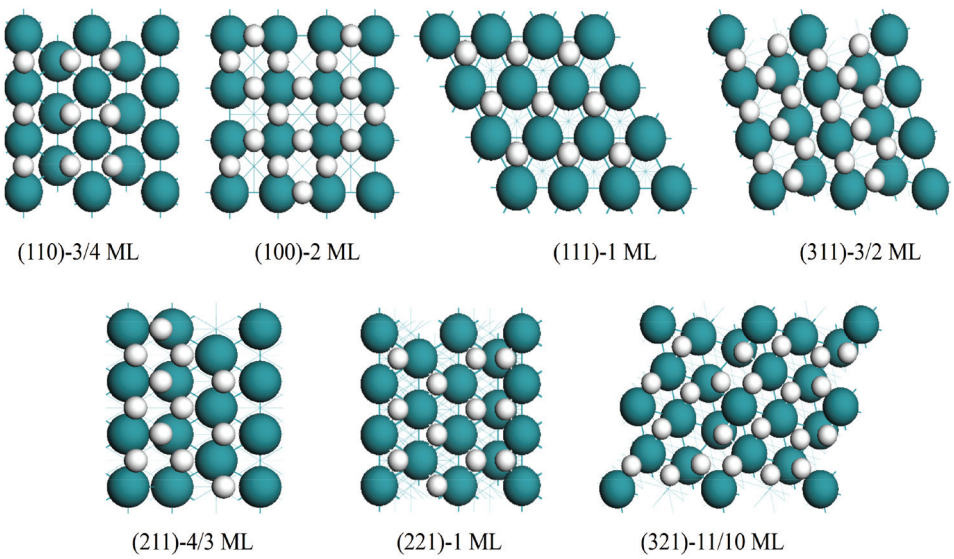

Fig. 1 Adsorption structures of hydrogen at saturation coverage on each Ru surface. The Ru atoms and adsorbed H atoms are colored dark green and white, respectively.

 This journal is © The Royal Society of Chemistry 2019

Published on 22 March 2019. Downloaded by SHANXI INSTITUTE OF COAL on 6/14/2019 4:02:46 AM.

Table 2 Adsorption energies and average Ru–H distance (d_{Ru-H}, Å) for the favorable adsorption sites for H on different Ru surfaces at the lowest coverage

Facet	Adsorption site	d_{Ru-H} (Å)	Adsorption energy (eV)
(110)	SB	1.79	−0.52
	$3F_1$	1.90	−0.43
	LB	1.98	−0.08
(100)	B	1.81	−0.61
	4F	2.05	−0.59
	T	1.63	−0.34
(111)	F	1.91	−0.60
	H	1.89	−0.53
	T	1.65	−0.12
(311)	B_1	1.82	−0.64
	$3F_1$	1.92	−0.48
	B_2	1.82	−0.46
	$3F_2$	1.91	−0.41
	T_2	1.69	−0.20
(211)	B_1	1.82	−0.65
	$3F_2$	1.91	−0.52
	$3F_4$	1.90	−0.52
	$3F_3$	1.89	−0.51
	B_5	1.82	−0.46
	T_1	1.65	−0.32
(221)	$3F_1$	1.91	−0.62
	$3F_3$	1.90	−0.56
	$3F_4$	1.89	−0.51
	$3F_2$	1.92	−0.45
	$3F_7$	1.94	−0.43
	$3F_5$	1.90	−0.42
	$3F_6$	1.93	−0.29
(321)	B_1	1.82	−0.59
	B_2	1.81	−0.53
	$3F_2$	1.91	−0.53
	B5	1.82	−0.49
	$3F_1$	1.92	−0.48
	$3F_3$	1.90	−0.46
	$3F_4$	1.89	−0.43
	$3F_5$	1.92	−0.37
	B_6	1.82	−0.29

erage induced strong repulsion between the adsorbed H atoms. For example on the Ru(110) surface, the partial H atoms located at the SB site would move to the stable $3F_1$ sites when the seventh H atom adsorbed onto the surface; on the Ru(321) surface, the B_5, $3F_1$, $3F_2$, $3F_4$ and $3F_5$ sites became possible and favorable on the surface, in addition to the most stable B_1 site at the lowest coverage. It should be noted that the stepwise adsorption energies show different degrees of decline with the increase of the hydrogen coverage. This is in line with the results[61] reported by Fernández, who reported that the reaction rate would decrease owing to the blockage of active sites if too much hydrogen is introduced. Moreover, some fluctuations in the stepwise adsorption energy can be found at higher coverage owing to the formation of a periodic structure, which strengthens the binding stability with the Ru surface.

As seen from Fig. 1, the results show that the saturation coverage depends on the surface stability, for example, the least stable Ru(100) surface has the highest saturated coverage (2 ML), followed by Ru(311) with 3/2 ML, Ru(321) with 11/10 ML, Ru(211) with 4/3 ML, Ru(221) with 1 ML, Ru(111) with 1 ML, and the lowest saturated coverage (3/4 ML) is found in Ru(110). As each Ru surface at the saturated coverage has different types of adsorbed H adsorption sites and each type of adsorbed hydrogen atom has similar adsorption configurations, as well as close stepwise adsorption energies. The distinct differences in the adsorbed H atom numbers and energies of these seven Ru surfaces indicate their different active sites and hydrogenation abilities, which are determined by the different Ru surface structures. The hydrogenation abilities of these Ru surfaces are reflected in the hybridization of the Ru d orbitals with the H s orbitals below the Fermi level, as shown in Fig. S12,† which in turn indicates the different interactions between the H atoms and Ru surfaces. In addition, the more available adsorption sites for the high Miller index surfaces mean that H adsorption reduces the surface symmetry. This is presumably owing to either the rearrangement of the H atoms or the change of the H atom adsorption sites caused by repulsive interactions.

3.3. Stable hydrogen coverage under different conditions

Using the F–G adsorption isotherm and the above data calculated at the DFT level, the variations of H coverage on the seven Ru surfaces were rationalized in terms of the temperature and H_2 partial pressure, as shown in Fig. 2. Each Ru surface has a characteristic color distribution region, each of which represents a possible equilibrium coverage at a given temperature and H_2 partial pressure. The red region represents the saturated hydrogen coverage, while the purple region represents the lowest hydrogen coverage. On these Ru surfaces, the hydrogen coverage monotonically decreases with the increasing temperature at a specified H_2 partial pressure while it raises with an increase in the H_2 partial pressure when the temperature is given.

Temperature and pressure have a great influence on the coverage of hydrogen. The saturated hydrogen coverage of the Ru(110), Ru(100), Ru(111), Ru(311), Ru(211), Ru(221) and Ru(321) surfaces are 1.99, 0.75, 0.99, 0.99, 1.49, 1.33, 1.00 and 1.10, respectively. Compared with conditions under vacuum, it is clear to see that the H coverage of the Ru(110), Ru(211) and Ru(221) surfaces increase significantly in low temperatures and high-pressure regions, especially that of the Ru(110) surface which increases much faster. Under the same conditions, the H coverage of the Ru(100), Ru(111) and Ru(311) surfaces decrease relatively, especially that of the Ru (100) surfaces which decrease a lot, while that of the Ru (321) surfaces remains unchanged. These variations can be attributed to the difference in surface stability and the repulsive interactions between the adsorbed H atoms caused by their distinct surface structure. Consequently, the hydrogen coverage can reflect the hydrogenation ability of each Ru surface, which is affected by the surface structure and active sites, as well as the surrounding environmental conditions.

As expected, the hydrogen desorption on these Ru surfaces is more convenient at high temperature and under low H_2 partial pressure. With increasing temperature, the downward trend of the isotherm slows down, which is consistent with

Published on 22 March 2019. Downloaded by SHANXI INSTITUTE OF COAL on 6/14/2019 4:02:46 AM.

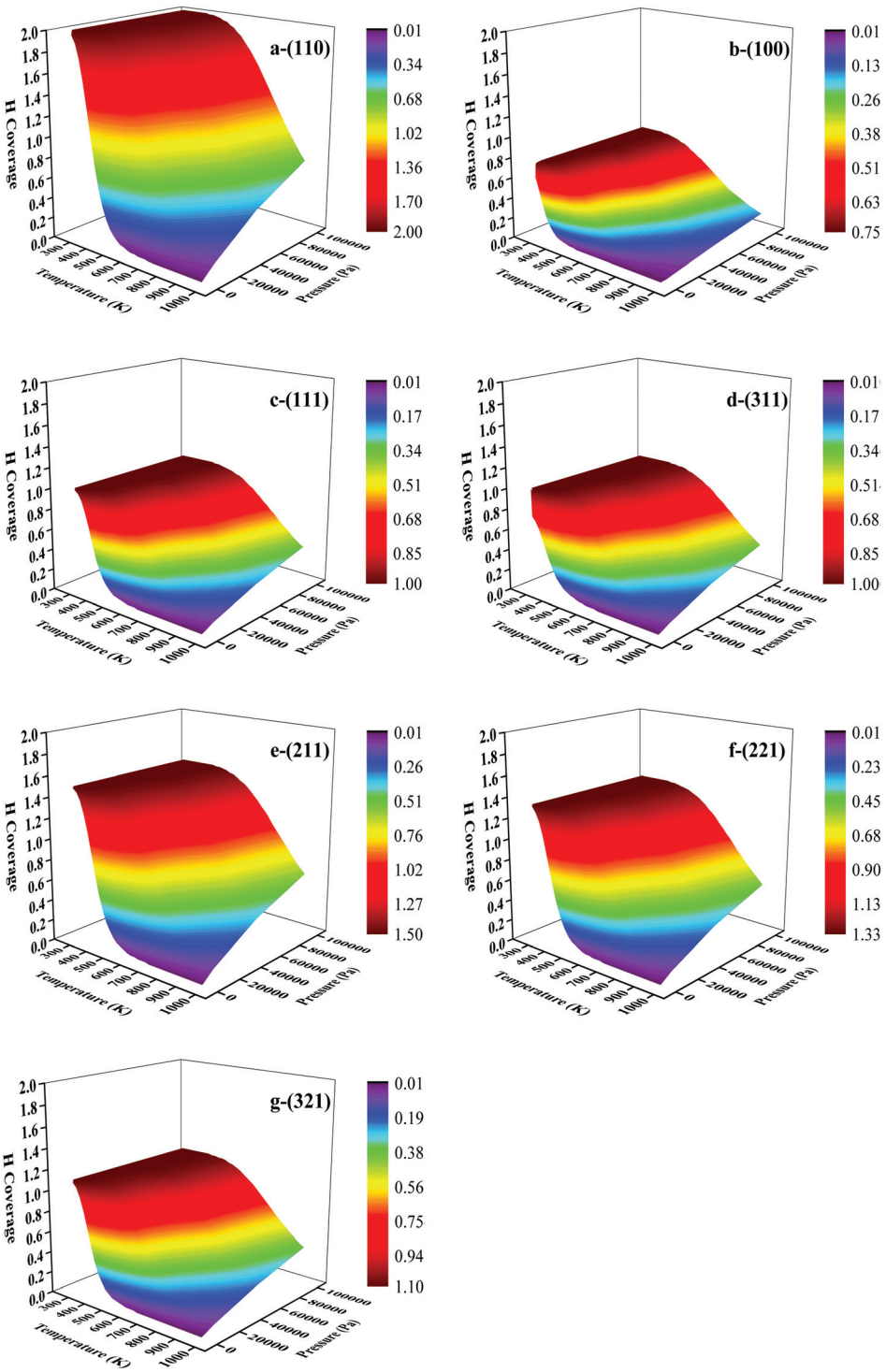

Fig. 2 Equilibrium phase diagrams of stable hydrogen coverage on different facets of Ru nanoparticles under different conditions: (a) Ru(110); (b) Ru(100); (c) Ru(111); (d) Ru(311); (e) Ru(211); (f) Ru(221); and (g) Ru(321).

that under a pressure of 10 000 Pa.[59] Under a H_2 partial pressure of 10 000 Pa, the full hydrogen desorption from these Ru surfaces (*i.e.* the bare surface is fully recovered) occurs mainly in the temperature ranges of 310–420 K, this is in line with the available temperature programmed desorption results (323–423 K).[61]

3.4. Morphology evolution of fcc Ru nanoparticles under hydrogen atmosphere

The morphology evolution of metal nanoparticles in a heterogeneous catalysis reaction is a key step to understand and control the real catalytic properties.[62–64] By applying the MSR

 This journal is © The Royal Society of Chemistry 2019

Published on 22 March 2019. Downloaded by SHANXI INSTITUTE OF COAL on 6/14/2019 4:02:46 AM.

model, one can account for realistic environmental conditions. In principle, hydrogen adsorption gives rise to anisotropic changes in the surface energy of the facets and thus affects the morphology of the fcc Ru nanocrystals. The equilibrium crystal morphologies of metal nanoparticles under different conditions were obtained using the minimum surface free energy, and the contribution of the crystal facets to the exposed surface area was determined using the surface free energy and orientation.

To clarify the effect of H adsorption on the morphology of Ru nanoparticles, fcc packed Ru nanoparticles with diameters of approximately 5 nm were chosen as they have been found to be the average size of Ru-based catalysts with a high performance for FTS.[65] To illustrate the morphology evolution of the constructed fcc Ru nanoparticles, the average coordination number of the surface atom sites was defined as:

$$\overline{\mathrm{CN}} = \sum_{i=1}^{\mathrm{surf}} \mathrm{CN}_i / N_{\mathrm{surf}} \quad (8)$$

In which CN_i is the coordination number of the ith surface atom site and N_{surf} is the total number of surface atom sites of the Ru nanoparticle. We treated two nanoparticles with $\overline{\mathrm{CN}}$ differences greater than 0.1 as different structures. The contour plot of the $\overline{\mathrm{CN}}$ of 5 nm fcc Ru nanoparticles under different conditions (the H_2 pressure varied from 0 to 10 0000 Pa and the temperature varied from 200 to 1000 K) is shown in Fig. 3a, and the typically constructed structures are shown in Fig. 3c. The corresponding surface energies for obtaining the Wulff shapes have been summarized in Table S1.†

At constant pressure, the shape of the fcc Ru nanoparticles changes from a rhombic dodecahedron to a truncated octahedron and the corresponding coordination number, $\overline{\mathrm{CN}}$, increases with the increase of the temperature (from the green region to the red region). The equilibrium morphology and contribution of the crystal facets to the exposed surface fraction (shown in Fig. 3b and Table S2†) under different conditions are quite different, and partially different from their shape under vacuum. The atmospheric pressure (10 0000 Pa) is used as an example, considering that this is the standard experimental condition for H_2 pretreatment.[66,67] With a temperature lower than 600 K, the Ru nanoparticle exhibits a rhombic dodecahedral shape with the (110) facets fully exposed, indicating that the (110) facet could be stabilized by hydrogen adsorption. At a higher temperature, the H coverage of the Ru surfaces decreases rapidly, and the fractions of Ru(110) are reduced at the expense of the production of new higher Miller index surfaces. When the temperature is greater than 600 K, the morphology of the fcc Ru is predominately dictated by the (110) and (211) facets. When the temperature increased from 700 to 900 K, the Ru(211) facet appears and occupies approximately a 17.2% to 91.9% fraction of the exposed total surface. Meanwhile, the Ru(111) and Ru(311) facet start to become exposed at 700 K, and a greater surface fraction can be found as the temperature further increases to 1000 K. The Ru(321) facet, which can be found on the equili-

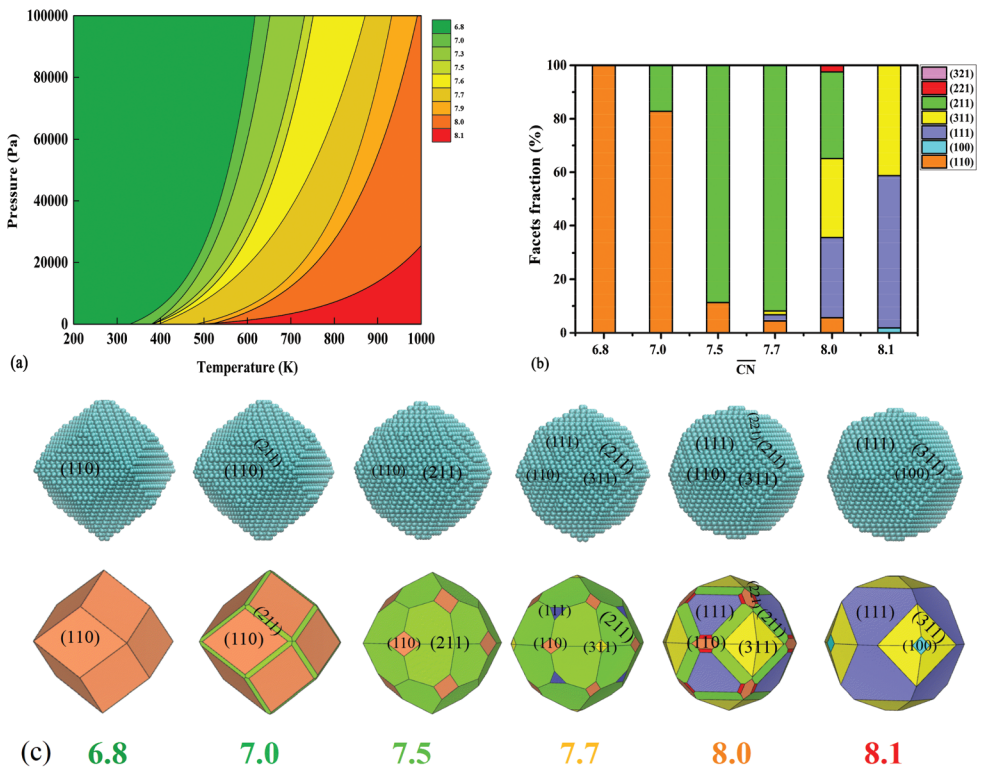

Fig. 3 (a) Contour plot of the $\overline{\mathrm{CN}}$ of 5 nm fcc Ru nanoparticles under different conditions. (b) The fractions of seven facets of typical Ru nanoparticles. (c) Typical structures of Ru nanoparticles under hydrogen atmosphere, marked with $\overline{\mathrm{CN}}$.

Published on 22 March 2019. Downloaded by SHANXI INSTITUTE OF COAL on 6/14/2019 4:02:46 AM.

brium shape of the fcc Ru nanoparticles under vacuum, does not appear in the studied H conditions, which indicates that it should not be considered as an active facet for Ru nanoparticles pretreated in H_2. The shape of the Ru nanoparticle with a $\overline{CN}$ of 8.0 and 8.1 exhibits a truncated octahedron, in agreement with the atomic structure of the fcc Ru nanoparticles confirmed using high-angle annular dark-field scanning transmission electron microscopy (HAADF STEM) analysis.[31] Obviously, hydrogen adsorption leads to dramatic changes in the surface morphology and the exposed facets of the fcc Ru nanocrystals. A high temperature and a low H_2 partial pressure can help to facilitate the exposure of the high Miller index surfaces.

It is reported that these open facets of fcc Ru with a relatively low activation energy of CO dissociation are responsible for the superior activity of the fcc Ru nanoparticles.[68] The origin of the high activity of the fcc Ru nanoparticles has been confirmed to stem from the higher active site density, especially from the (111) facet.[42,69] Despite the fact that the (111) facet contributes the largest area to the Ru nanoparticle in a vacuum, the operability of the experiment is very difficult to achieve. At higher temperatures, the $\overline{CN}$ of the Ru nanoparticle becomes large, corresponding to the increased exposed facets. From Fig. 3c, it can be seen that the Ru(111) facet does not exist in the Ru nanoparticles with a lower $\overline{CN}$ (6.8–7.5). In the Ru nanoparticles with a $\overline{CN}$ of 7.7, the Ru(111) facet only covers a 2.2% fraction of the exposed total surface. The proportion of the exposed Ru(111) facet with a $\overline{CN}$ of 8.0 and 8.1 under hydrogen atmosphere is found to account for approximately 29.9% and 56.8%, taking up most of the surface area with a high density of the active sites. It can be predicted that more active (111) facets would be exposed at a higher temperature. Accordingly, the abundant active (111) facets are expected to endow the fcc Ru nanoparticles with a better catalytic performance. The results show that both the maneuverability of the experiment and the large surface proportion of (111) exposure can be controlled at a high temperature and low pressure, ensuring the higher catalytic activity of the Ru nanoparticles upon hydrogen adsorption. Thus, tuning the desired morphology and exposed facets of the Ru nanoparticles can be achieved by changing the temperature and pressure conditions, which is very useful for improving the catalytic activity.

4. Conclusion

Applying the MSR model, the equilibrium morphology of a fcc Ru nanoparticle was studied upon hydrogen adsorption in detail. The identified stable configurations and energies show that the hydrogen adsorption strength and saturation coverage on each surface are significantly different owing to their distinct surface structures and active sites. The phase diagram for each facet was constructed to describe the hydrogen equilibrium coverage at given temperatures and pressures. It was found that the morphologies and the exposed facets of the fcc Ru nanoparticles highly depend on the H_2 pressure and temperature. The result shows that high temperature and low H_2 partial pressure treatment can facilitate the exposure of the (111) facets with abundant active sites to improve the reactivity of Ru nanoparticles. More importantly, we found that the (110) facet does not occur under vacuum, but has a large fraction under certain H_2 pressures at low temperatures. This shows that analysis of the catalytic properties using the MSR model is necessary to obtain real information in working conditions. Our work provides a useful guide for tuning the shape of Ru nanoparticles by means of controlling the H_2 conditions and paves the way for the rational design of Ru nanocatalysts.

Conflicts of interest

There are no conflicts of interest to declare.

Acknowledgements

The work was supported by the National Natural Science Foundation of China (No. 21736007, 21872162, 11604357, and U1710104), the Natural Science Foundation of Shanghai (16ZR1443200), the Youth Innovation Promotion Association CAS, the ShanXi Provincial Research Foundation for Basic Research (No. 201701D221242), and the "Transformational Technologies for Clean Energy and Demonstration", Strategic Priority Research Program of the Chinese Academy of Sciences (No. XDA 21020202). The authors are grateful to Lvliang's cloud computing center for computational resources by the Tianhe-2.

References

1 C. Chen, Y. Kang, Z. Huo, Z. Zhu, W. Huang, H. L. Xin, J. D. Snyder, D. Li, J. A. Herron, M. Mavrikakis, M. Chi, K. L. More, Y. Li, N. M. Markovic, G. A. Somorjai, P. Yang and V. R. Stamenkovic, *Science*, 2014, **343**, 1339–1343.
2 M. T. Koper, *Nanoscale*, 2011, **3**, 2054–2073.
3 H. H. Li, S. Y. Ma, Q. Q. Fu, X. J. Liu, L. Wu and S. H. Yu, *J. Am. Chem. Soc.*, 2015, **137**, 7862–7868.
4 N. S. Porter, H. Wu, Z. Quan and J. Fang, *Acc. Chem. Res.*, 2013, **46**, 1867–1877.
5 J. Watt, C. Yu, S. L. Chang, S. Cheong and R. D. Tilley, *J. Am. Chem. Soc.*, 2013, **135**, 606–609.
6 Z. Li, T. Lin, F. Yu, Y. An, Y. Dai, S. Li, L. Zhong, H. Wang, P. Gao and Y. Sun, *ACS Catal.*, 2017, **7**, 8023–8032.
7 K. Zhou and Y. Li, *Angew. Chem., Int. Ed.*, 2012, **51**, 602–613.
8 C. Fernandez, N. Bion, E. M. Gaigneaux, D. Duprez and P. Ruiz, *J. Catal.*, 2016, **344**, 16–28.
9 F. Zaera, *ACS Catal.*, 2017, **7**, 4947–4967.
10 W. Zang, G. Li, L. Wang and X. Zhang, *Catal. Sci. Technol.*, 2015, **5**, 2532–2553.

 This journal is © The Royal Society of Chemistry 2019

Published on 22 March 2019. Downloaded by SHANXI INSTITUTE OF COAL on 6/14/2019 4:02:46 AM.

11 Z. Fan and H. Zhang, *Chem. Soc. Rev.*, 2016, **45**, 63–82.
12 N. T. Khi, J. Park, H. Baik, H. Lee, J. H. Sohn and K. Lee, *Nanoscale*, 2015, **7**, 3941–3946.
13 J. Pal and T. Pal, *Nanoscale*, 2015, **7**, 14159–14190.
14 J.-J. Liu, Y. Meng, P. Ren, B. Zhaorigetu, W. Guo, D.-B. Cao, Y.-W. Li, H. Jiao, Z. Liu, M. Jia, Y. Yang, A. Xu and X.-D. Wen, *Catal. Today*, 2017, **282**, 96–104.
15 S. Cheong, J. D. Watt and R. D. Tilley, *Nanoscale*, 2010, **2**, 2045–2053.
16 B. T. Sneed, A. P. Young and C. K. Tsung, *Nanoscale*, 2015, **7**, 12248–12265.
17 S. W. T. Price, D. J. Martin, A. D. Parsons, W. A. Slawinski, A. Vamvakeros, S. J. Keylock, A. M. Beale and J. F. W. Mosselmans, *Sci. Adv.*, 2017, **3**, 1602838–1602838.
18 X. Zhang, J. Meng, B. Zhu, J. Yu, S. Zou, Z. Zhang, Y. Gao and Y. Wang, *Chem. Commun.*, 2017, **53**, 13213–13216.
19 K. Høydalsvik, J. B. Fløystad, A. Voronov, G. J. B. Voss, M. Esmaeili, J. Kehres, H. Granlund, U. Vainio, J. W. Andreasen, M. Rønning and D. W. Breiby, *J. Phys. Chem. C*, 2014, **118**, 2399–2407.
20 S. B. Vendelbo, C. F. Elkjaer, H. Falsig, I. Puspitasari, P. Dona, L. Mele, B. Morana, B. J. Nelissen, R. van Rijn, J. F. Creemer, P. J. Kooyman and S. Helveg, *Nat. Mater.*, 2014, **13**, 884–890.
21 K. Qadir, S. H. Joo, B. S. Mun, D. R. Butcher, J. R. Renzas, F. Aksoy, Z. Liu, G. A. Somorjai and J. Y. Park, *Nano Lett.*, 2012, **12**, 5761–5768.
22 H. J. Qiu, H. T. Xu, L. Liu and Y. Wang, *Nanoscale*, 2015, **7**, 386–400.
23 A. Banerjee, V. Navarro, J. W. Frenken, A. P. van Bavel, H. P. Kuipers and M. Saeys, *J. Phys. Chem. Lett.*, 2016, **7**, 1996–2001.
24 S. B. Simonsen, I. Chorkendorff, S. Dahl, M. Skoglundh, K. Meinander, T. N. Jensen, J. V. Lauritsen and S. Helveg, *J. Phys. Chem. C*, 2012, **116**, 5646–5653.
25 T. Wang, X. Tian, Y. Yang, Y.-W. Li, J. Wang, M. Beller and H. Jiao, *J. Phys. Chem. C*, 2016, **120**, 2846–2854.
26 Q. Shi and R. Sun, *Comput. Theor. Chem.*, 2017, **1106**, 43–49.
27 T. Wang, X. Tian, Y. Yang, Y.-W. Li, J. Wang, M. Beller and H. Jiao, *Surf. Sci.*, 2016, **651**, 195–202.
28 B. Zhu, J. Meng and Y. Gao, *J. Phys. Chem. C*, 2017, **121**, 5629–5634.
29 T. Wang, S. Wang, Q. Luo, Y.-W. Li, J. Wang, M. Beller and H. Jiao, *J. Phys. Chem. C*, 2014, **118**, 4181–4188.
30 T. Wang, X. Tian, Y. Yang, Y.-W. Li, J. Wang, M. Beller and H. Jiao, *Phys. Chem. Chem. Phys.*, 2016, **18**, 6005–6012.
31 E. K. Abo-Hamed, T. Pennycook, Y. Vaynzof, C. Toprakcioglu, A. Koutsioubas and O. A. Scherman, *Small*, 2014, **10**, 3145–3152.
32 K. Kusada and H. Kitagawa, *Adv. Mater.*, 2016, **28**, 1129–1142.
33 Y. Fang, J. Li, T. Togo, F. Jin, Z. Xiao, L. Liu, H. Drake, X. Lian and H.-C. Zhou, *Chem*, 2018, **4**, 555–563.
34 K. Kusada, H. Kobayashi, T. Yamamoto, S. Matsumura, N. Sumi, K. Sato, K. Nagaoka, Y. Kubota and H. Kitagawa, *J. Am. Chem. Soc.*, 2013, **135**, 5493–5496.
35 L. Kumara, O. Sakata, S. Kohara, A. Yang, C. Song, K. Kusada, H. Kobayashi and H. Kitagawa, *Phys. Chem. Chem. Phys.*, 2016, **18**, 30622–30629.
36 C. Song, O. Sakata, L. S. Kumara, S. Kohara, A. Yang, K. Kusada, H. Kobayashi and H. Kitagawa, *Sci. Rep.*, 2016, **6**, 31400.
37 Y. Yao, D. S. He, Y. Lin, X. Feng, X. Wang, P. Yin, X. Hong, G. Zhou, Y. Wu and Y. Li, *Angew. Chem., Int. Ed.*, 2016, **55**, 5501–5505.
38 H. Ma and C. Na, *ACS Catal.*, 2015, **5**, 1726–1735.
39 M. Zhao, L. Figueroa-Cosme, A. O. Elnabawy, M. Vara, X. Yang, L. T. Roling, M. Chi, M. Mavrikakis and Y. Xia, *Nano Lett.*, 2016, **16**, 5310–5317.
40 M. Zhao, A. O. Elnabawy, M. Vara, L. Xu, Z. D. Hood, X. Yang, K. D. Gilroy, L. Figueroa-Cosme, M. Chi and M. Mavrikakis, *Chem. Mater.*, 2017, **29**, 9227–9237.
41 N. M. AlYami, A. P. LaGrow, K. S. Joya, J. Hwang, K. Katsiev, D. H. Anjum, Y. Losovyj, L. Sinatra, J. Y. Kim and O. M. Bakr, *Phys. Chem. Chem. Phys.*, 2016, **18**, 16169–16178.
42 W.-Z. Li, J.-X. Liu, J. Gu, W. Zhou, S.-Y. Yao, R. Si, Y. Guo, H.-Y. Su, C.-H. Yan, W.-X. Li, Y.-W. Zhang and D. Ma, *J. Am. Chem. Soc.*, 2017, **139**, 2267–2276.
43 A. Comas-Vives, K. Furman, D. Gajan, M. C. Akatay, A. Lesage, F. H. Ribeiro and C. Copéret, *Phys. Chem. Chem. Phys.*, 2016, **18**, 1969–1979.
44 Z. Fan and H. Zhang, *Acc. Chem. Res.*, 2016, **49**, 2841–2850.
45 A.-X. Yin, W.-C. Liu, J. Ke, W. Zhu, J. Gu, Y.-W. Zhang and C.-H. Yan, *J. Am. Chem. Soc.*, 2012, **134**, 20479–20489.
46 H. J. Monkhorst and J. D. Pack, *Phys. Rev. B: Solid State*, 1976, **13**, 5188.
47 G. Kresse and J. Hafner, *Phys. Rev. B: Condens. Matter Mater. Phys.*, 1993, **47**, 558.
48 G. Kresse and J. Furthmüller, *Phys. Rev. B: Condens. Matter Mater. Phys.*, 1996, **54**, 11169.
49 P. E. Blöchl, *Phys. Rev. B: Condens. Matter Mater. Phys.*, 1994, **50**, 17953.
50 J. P. Perdew, K. Burke and M. Ernzerhof, *Phys. Rev. Lett.*, 1996, **77**, 3865.
51 B. Zhu, Z. Xu, C. Wang and Y. Gao, *Nano Lett.*, 2016, **16**, 2628–2632.
52 J. Meng, B. E. Zhu and Y. Gao, *J. Phys. Chem. C*, 2018, **122**, 6144–6150.
53 M. Duan, J. Yu, J. Meng, B. Zhu, Y. Wang and Y. Gao, *Angew. Chem., Int. Ed.*, 2018, **57**, 6464–6469.
54 M. W. Chase, J. L. Curnutt, J. R. Downey, R. A. McDonald, A. N. Syverud and E. A. Valenzuela, *J. Phys. Chem. Ref. Data*, 1982, **11**, 695–940.
55 Y. Nanba, T. Ishimoto and M. Koyama, *J. Phys. Chem. C*, 2017, **121**, 27445–27452.
56 E. Waldt, R. Ahlrichs, M. M. Kappes and D. Schooss, *ChemPhysChem*, 2014, **15**, 862–865.

Published on 22 March 2019. Downloaded by SHANXI INSTITUTE OF COAL on 6/14/2019 4:02:46 AM.

57 A. Comas-Vives, K. Furman, D. Gajan, M. C. Akatay, A. Lesage, F. H. Ribeiro and C. Coperet, *Phys. Chem. Chem. Phys.*, 2016, **18**, 1969–1979.
58 R. Berthoud, P. Délichère, D. Gajan, W. Lukens, K. Pelzer, J.-M. Basset, J.-P. Candy and C. Copéret, *J. Catal.*, 2008, **260**, 387–391.
59 X. Shen, L.-J. Garces, Y. Ding, K. Laubernds, R. P. Zerger, M. Aindow, E. J. Neth and S. L. Suib, *Appl. Catal., A*, 2008, **335**, 187–195.
60 S. Zhao, X.-W. Liu, C.-F. Huo, X.-D. Wen, W. Guo, D. Cao, Y. Yang, Y.-W. Li, J. Wang and H. Jiao, *Catal. Today*, 2016, **261**, 93–100.
61 C. Fernández, C. Pezzotta, E. M. Gaigneaux, N. Bion, D. Duprez and P. Ruiz, *Catal. Today*, 2015, **251**, 88–95.
62 K. Lee, M. Kim and H. Kim, *J. Mater. Chem.*, 2010, **20**, 3791.
63 P. Ann Lin, B. Natarajan, M. Zwolak and R. Sharma, *Nanoscale*, 2018, **10**, 4528–4537.
64 L. Liu, M. Yu, Q. Wang, B. Hou, Y. Liu, Y. Wu, Y. Yang and D. Li, *Catal. Sci. Technol.*, 2018, **8**, 2728–2739.
65 J. Chen, J. Li, Y. Zhao, Y. Zhang and J. Hong, *J. Nat. Gas Chem.*, 2012, **21**, 673–679.
66 K. Xiong, J. Li, K. Liew and X. Zhan, *Appl. Catal., A*, 2010, **389**, 173–178.
67 S. Chen, J. Li, Y. Zhang, Y. Zhao, K. Liew and J. Hong, *Top. Catal.*, 2013, **57**, 437–444.
68 J.-X. Liu, P. Wang, W. Xu and E. J. M. Hensen, *Engineering*, 2017, **3**, 467–476.
69 J. Gu, Y. Guo, Y.-Y. Jiang, W. Zhu, Y.-S. Xu, Z.-Q. Zhao, J.-X. Liu, W.-X. Li, C.-H. Jin, C.-H. Yan and Y.-W. Zhang, *J. Phys. Chem. C*, 2015, **119**, 17697–17706.

This journal is © The Royal Society of Chemistry 2019